Eccentricity-paced atmospheric carbon-dioxide variations across the middle Miocene climate transition

Markus Raitzsch[1,2], Jelle Bijma[2], Torsten Bickert[1], Michael Schulz[1], Ann Holbourn[3], Michal Kučera[1]

[1]MARUM – Zentrum für Marine Umweltwissenschaften, Universität Bremen, Leobener Straße, 28359 Bremen, Germany
[2]Alfred-Wegener-Institut, Helmholtz-Zentrum für Polar-und Meeresforschung, Am Handelshafen 12, 27570, Bremerhaven, Germany
[3]Christian-Albrechts-Universität, Institut für Geowissenschaften, 24118 Kiel, Germany

Correspondence to: Markus Raitzsch (mraitzsch@marum.de)

Abstract. The middle Miocene climate transition ~14 Ma marks a fundamental step towards the current "icehouse" climate, with a ~1 ‰ $\delta^{18}O$ increase and a ~1 ‰ transient $\delta^{13}C$ rise in the deep ocean, indicating rapid expansion of the East Antarctic Ice Sheet associated with a change in the operation of the global carbon cycle. The variation of atmospheric CO_2 across the carbon-cycle perturbation has been intensely debated as proxy records of pCO_2 for this time interval are sparse and partly contradictory. Using boron isotopes ($\delta^{11}B$) in planktonic foraminifers from drill site ODP 1092 in the South Atlantic, we show that long-term pCO_2 variations between ~14.3 and 13.2 Ma were paced by 400 k.y. eccentricity cycles, with decreasing pCO_2 at high eccentricity and vice versa. Our data support results from a carbon-cycle model study, according to which increased monsoon intensity at high eccentricity enhanced weathering and river fluxes in the tropics, resulting in increasing carbonate and organic carbon burial and hence decreasing atmospheric CO_2. In this scenario, a combination of the eccentricity-driven climatic cycle and enhanced meridional deep-ocean circulation during Antarctic ice-sheet expansion may have both contributed to the pCO_2 rise following Antarctic glaciation, acting as a negative feedback on the progressing glaciation and helping to stabilize the climate system on its way to the late Cenozoic "icehouse" world.

1 Introduction

With rapid cooling of Antarctica and associated expansion of the East Antarctic Ice Sheet (EAIS), the middle Miocene climate transition (MMCT) ~14 Ma marks a fundamental step towards the current "icehouse" climate (Woodruff and Savin, 1991; Flower and Kennett, 1994). The transition is characterized by a $\delta^{18}O$ increase of ~1 ‰ in the deep ocean between 13.9 and 13.8 Ma and a positive (~1 ‰) $\delta^{13}C$ excursion between 13.9 and 13.5 Ma indicating a fundamental change in global carbon-cycle dynamics (Shevenell et al., 2004; Holbourn et al., 2005, 2007). The carbon-isotope maximum (CM) event CM6 is the last and most prominent of at least six maxima within a long-lasting $\delta^{13}C$ excursion, the "Monterey Excursion", spanning ~16.9 to ~13.5 Ma and apparently paced by long-term changes in the 400 k.y. eccentricity cycle of the Earth's orbit (Vincent and Berger, 1985; Holbourn et al., 2007). These $\delta^{13}C$ maxima hint at a major reorganization of the marine carbon

Climate
of the Past
Discussions

30   cycle, and the temporal coincidence of CM6 with expansion of the Antarctic ice sheet indicates that the glaciation may have
been caused by cooling due to reduced CO_2 radiative forcing (Greenop et al., 2014).

The CM events within the Monterey Excursion have been traditionally considered as episodes of increased organic-carbon
(C_{org}) burial resulting in ^{12}C-depleted seawater, atmospheric CO_2 drawdown and associated cooling and buildup of
continental ice (Vincent and Berger, 1985; Flower and Kennett, 1993, 1994; Badger et al., 2013). In a recent study, it was

35   proposed that a more sluggish meridional Pacific Ocean overturning circulation, due to reduced deep-water formation in the
Southern Ocean, enhanced the weathering of ^{13}C-enriched shelf carbonates, and that the expansion of the terrestrial carbon
reservoir may have been responsible for the $\delta^{13}C$ excursion CM6, associated with a decrease in pCO$_2$ (Ma et al., 2018).
Another explanation for the CM events refers to the "missing sink" mechanism (Lear et al., 2004), where large areas of
Antarctic silicate rocks are covered by ice caps, which reduce chemical weathering and, thus, limit their potential as a sink

40   for atmospheric CO_2 (Pagani et al., 1999; Lear et al., 2004; Shevenell et al., 2008). While all scenarios result in increasing
marine $\delta^{13}C$, the former two act as positive feedbacks (falling CO_2) promoting ice-sheet expansion, and the latter as a
negative feedback (rising CO_2) preventing global climate from evolving to an even colder state.

The nature of the carbon cycle perturbation could be better constrained if we knew the evolution of atmospheric CO_2 across
the MMCT. Understanding the role of the carbon cycle in this cooling step is a key to assess Earth-system sensitivity to CO_2

45   forcing and the long-term stability of the Antarctic ice sheet under rising CO_2 concentrations. However, most proxy records
for the history of pCO$_2$ across the MMCT are incomplete or at low resolution, thus prohibiting resolution of the CM events
(Pagani et al., 1999; Kürschner et al., 2008; Foster et al., 2012; Ji et al., 2018; Sosdian et al., 2018; Super et al., 2018) and
making it difficult to identify the mechanism responsible for the major step into the "icehouse" world. The only high-
resolution pCO$_2$ reconstruction across CM6 is based on alkenone $\delta^{13}C$ data from a Miocene outcrop on Malta (Badger et al.,

50   2013), but it does not reveal a significant change.

Therefore, to better understand atmospheric CO_2 evolution over the period of EAIS growth, we generated a high-resolution
reconstruction based on $\delta^{11}B$ measurements of fossil planktonic foraminifers from the South Atlantic (Figs. 1, 2). The boron
isotopic composition of biogenic carbonates is a reliable recorder of ambient pH, which in turn is closely linked to
atmospheric pCO$_2$ in oligotrophic surface waters. Our record fully captures the carbon isotope excursions CM5b and CM6,

55   which include the major expansion of the EAIS.

1 Material and Methods

1.1 Sampling strategy

This research used samples from Ocean Drilling Program (ODP) Site 1092, located at 46.41 S and 7.08 E (Fig. 1) in a water
depth of 1973 m. The interval studied (~178-184 mcd, see Table S1) consists of nannofossil ooze with excellent carbonate

60   preservation, as shown by SEM-imaged undissolved coccoliths, which are susceptible to corrosion (Fig. 2). The shown
example is from ~13.8 Ma, where pH was low, but shell preservation is similarly good throughout the entire record.

Approximately 200 specimens of the cold-water dwelling planktonic foraminifer *G. bulloides* were picked for $\delta^{11}B$ analysis from 35 processed 10 cm^3 sediment samples. In addition, about 5 to 8 specimens of the benthic foraminifer *Cibicidoides wuellerstorfi* were picked from 14 intervals to reconstruct deep-sea pH (Table S1). Today, surface-water pCO_2 at Site 1092

65 is close to equilibrium with the atmosphere ($\Delta pCO_{2sea-air} < -30$ µatm (Takahashi et al., 1993, 2009)). Plankton tow data revealed that *G. bulloides* generally lives within the upper 100 m of the water column (Mortyn and Charles, 2003). Based on DIC (dissolved inorganic carbon) and TA (total alkalinity) from seasonal TCO2+TALK (Goyet et al., 2000), and temperature and salinity from WOA13 data sets, modern gradients in pH and pCO_2 are small at this site within the upper 200 m of the water column. During the austral spring season, when the shell flux of *G. bulloides* is highest (Jonkers and Kučera,

70 2015; Raitzsch et al., 2018), the differences in pH and pCO_2 within this depth range are -0.03 and 17 µatm, respectively. Hence, we expect *G. bulloides* to be a reliable recorder of subsurface pH and pCO_2.

1.2 Age model

The age model used in this study is adopted from Kuhnert et al. (2009), but was revised to bring it in line with the astronomically tuned stable isotope record of the reference IODP Site U1338 (Holbourn et al., 2014) (Fig. 3, Table S2). In

75 addition, chron C5ADn (top) identified at 182.51 mcd and originally dated to 14.178 Ma (Censarek and Gersonde, 2002) was tied to 14.081 Ma from the age model of Site U1338 (Holbourn et al., 2014). For direct comparison of our pCO_2 record with the boron-based reconstructions available from the literature, the age models of ODP 761 (Holbourn et al., 2004, Foster et al., 2012, Sosdian et al., 2018) and the Blue Clay Formation of Ras-il-Pellegrin on Malta (Abels et al., 2005; Badger et al., 2013) were also re-tuned to match the reference curve U1338 (Table S2). Based on these revised age models, the $\delta^{18}O$ and

80 $\delta^{13}C$ profiles of Sites 1092, ODP 791 and the Blue Clay Formation generally show a good agreement with those of Site U1338 (Fig. 3).

1.3 Boron isotope analysis

Foraminifer shells were cleaned following the protocol of Barker et al. (2003). Trace metal and boron isotope ($\delta^{11}B$) were measured following Raitzsch et al. (2018). Briefly, the cleaned samples were dissolved in 60 µL of 1 N HNO_3 and micro-

85 distilled on a hotplate to separate boron from the carbonate matrix. The microdistillation method has been proven to yield a B recovery of ~100 %, a low procedural blank, and accurate results, even at low B concentrations (Gaillardet et al., 2001; Wang et al., 2010; Misra et al., 2014; Raitzsch et al., 2018). The distillate containing only boron was diluted with 2 % HNO_3 and analyzed for isotopes in triplicate using a Nu Plasma II multi-collector ICPMS at AWI (Bremerhaven, Germany) that is equipped with a customized detector array of 16 Faraday cups and 6 secondary electron multipliers (SEM), also termed ion

90 counters (IC). ^{11}B and ^{10}B were collected in IC5 and IC0, respectively, at a boron concentration of ~3 ppb. As three of the SEMs were later replaced by Daly detectors, ^{11}B and ^{10}B of *C. wuellerstorfi* samples were collected in D5 and D0, respectively, at a boron concentration of ~2 ppb. $^{11}B/^{10}B$ was standardized against concentration-matched NBS 951 using the standard-sample-standard bracketing technique, and frequent analysis of control standard AE121 with an isotopic

Climate
of the Past
Discussions

composition similar to that of foraminifers was monitored to ensure accuracy of measurement. Measurement uncertainties

95 are reported as 2 standard deviations (2σ) derived from triplicate measurements or as ±0.30 ‰ (for SEM-analyzed samples) and ±0.25 ‰ (for Daly-analyzed samples) determined from the long-term reproducibility (2σ) of the control standard, whichever is larger (see Table S1).

1.4 Reconstruction of pH and pCO$_2$ from δ^{11}B

Planktonic δ^{11}B was converted to sea-surface pH (Fig. S1) using the δ^{11}B$_{foram}$/δ^{11}B$_{borate}$ relationship for *G. bulloides* (Raitzsch

100 et al., 2018), where δ^{11}B$_{borate}$ is determined by the dissociation constant pK$_B$ and δ^{11}B$_{seawater}$. pK$_B$ is dependent on salinity, temperature and pressure. Mg/Ca was taken from Kuhnert et al. (2009) for temperature estimates, and pressure was chosen from 50 m water depth, the assumed average calcification depth of *G. bulloides*. To account for seawater Mg/Ca, which was approximately 3.2 mol/mol ~14 Ma ago (Stanley and Hardie, 1999; Horita et al., 2002), Mg/Ca temperatures were corrected by applying a correction factor of 0.825 to the pre-exponential constant of the Mg/Ca-temperature equation of Mashiotta et

105 al. (1999). This correction factor was previously determined for *G. sacculifer* by Evans and Müller (2012), but we assume that the effect of seawater Mg/Ca on shell Mg/Ca is similar for *G. bulloides*, since both have similar Mg/Ca ratios. However, the difference between Mg/Ca$_{sw}$-corrected and non-corrected Mg/Ca absolute temperatures is in the order of 1.7 °C, but the relative changes are nearly identical.

Relative salinity changes were estimated by converting δ^{18}O$_{sw}$, derived from planktonic foraminiferal δ^{18}O and Mg/Ca

110 temperatures (Shackleton, 1974), to salinity using a δ^{18}O$_{sw}$:salinity gradient of 1.1 ‰ (the change in δ^{18}O$_{sw}$ per salinity unit). This minimum gradient is required to keep the upper ocean density difference across the Subantarctic Front to enable the formation of Antarctic Intermediate Water (Kuhnert et al., 2009), which existed as Southern Component Intermediate Water (SCIW) since at least ~16 Ma (Shevenell and Kennett, 2004) and spread into all oceans adjacent to the Southern Ocean (Wright et al., 1992). However, since the computed absolute salinity values are unrealistically low, an offset of 17.2 (psu)

115 was added to the entire salinity record to achieve post-glaciation values similar to today. The reconstructed relative salinity change across the MMCT at Site 1092 is slightly more than 1 (psu), which is eqiavalent to the salinity gradient across the Subantarctic front today. Deep-sea pH from *C. wuellerstorfi* δ^{11}B$_{foram}$ shown in Fig. S1 was calculated using a δ^{11}B$_{foram}$:δ^{11}B$_{borate}$ relationship of 1:1 (Rae et al., 2011), deep-sea temperatures derived from Mg/Ca (data courtesy of H. Kuhnert) using the species-specific calibration of Raitzsch et al. (2008), a salinity of 34 (psu), and a paleo-water depth of

120 1794 m.

The most critical parameter for correct conversion to pH is δ^{11}B$_{seawater}$, which is fortunately well constrained for the middle Miocene. We used a δ^{11}B$_{seawater}$ value of 37.80 ‰, which is the mean value from different independent studies and in close agreement with each other to within 0.1 ‰ (1σ) (Pearson and Palmer, 2000; Foster et al., 2012; Raitzsch and Hönisch, 2013; Greenopet al., 2017), and also comparable to the 38.5 ‰ modeled by Lemarchand et al. (2000).

125 To calculate pCO$_2$ from sea-surface pH, a second carbonate system parameter needs to be constrained. For this study, we used a sea-surface TA of 2000 μmol/kg, which is in line with various carbon cycle model results (Tyrrell and Zeebe, 2004;

Ridgwell, 2005; Caves et al., 2016; Sosdian et al., 2018, Zeebe and Tyrrell, 2019), and what we applied to the entire record. However, to verify the validity of our approach we tested the effect of varying TA on pCO_2 calculations (see section 3.2).

To assess whether a pH effect on Mg/Ca-derived temperatures and, in turn, pH-corrected temperature influences estimated

130   pCO_2 as shown by Gray and Evans (2019), we used a slightly modifed version of their 'MgCaRB' package written in 'R'. Briefly, this program corrects Mg/Ca for the effects of salinity and pH and the resulting change in the temperature effect on pK_B and hence on pH, until the change in both parameters between two iterations fall below certain threshold values. The original R code from Gray and Evans (2019) uses sediment age and associated error to determine past salinity and its uncertainty, based on the secular seawater salinity model from Spratt and Lisiecki (2016). Hence, the model is limited to the

135   last ~800 ka. To adopt the code for our Miocene study, we slightly modified 'MgCaRB.d11B.R' from Gray and Evans (2019) by allowing for directly use estimated salinies and associated uncertainties. In addition, the seawater B isotopic composition was changed from 39.61 ‰ to the Miocene value of 37.80 ‰ (see code in the supplement). While the Miocene relative salinity variations can be constrained from changes in benthic foraminiferal $\delta^{18}O$, the absolute salinity levels are difficult to determine. Hence this approach only allows for comparing relative differences between the conventionally and

140   the iteratively corrected pCO_2 estimates. For this reason, the temperature and pCO_2 values of the two approaches were brought in coincidence at the start of the record (Fig. S2).

Uncertainties of pCO_2 estimates were fully propagated from individual uncertainties in pH (converted from 2σ measurement uncertainty of $\delta^{11}B$), TA (±100 µmol/kg), temperature (±1 °C), and salinity (±1 psu) using the 'seacarb' package (Lavigne et al., 2011) programmed in 'R'. The applied temperature uncertainty is similar to the mean difference of ~2 °C between the

145   non-corrected and pH-corrected Mg/Ca temperatures (Fig. S2), while the TA uncertainty is similar to the mean standard deviation of ±~130 µmol/kg between different TA models and clearly encompassing the standard deviation of ±~50 µmol/kg for each model across the MMCT (Sosdian et al., 2018). The applied salinity uncertainty encompasses the potential salinity change across the MMCT. We did not apply uncertainties for Mg/Ca$_{sw}$ and $\delta^{11}B_{sw}$, since both are systematic errors and would just shift the pCO_2 record in either direction.

3. Results

3.1 Carbon dioxide record

Our boron-based record indicates a steady pCO_2 increase from ~390 to 520 ± 60 µatm between 14.25 and 14.08 Ma and a subsequent decrease to ~360 µatm until 13.87 Ma, culminating after the onset of the major ice-sheet expansion (Fig. 4E). It should be noted that this ~160 µatm drop in pCO_2 occurred at a time of northward shifting Southern Ocean fronts, which is

155   only related to a step-like drop in sea-surface temperature (SST) and salinity around 14 Ma at this site (Fig. 4C) (Kuhnert et al., 2009). At 13.82 Ma, when SST had already reached a lower stable level and after the inception of the ~1 ‰ rise in benthic $\delta^{18}O$ (Fig. 4A), pCO_2 increased rapidly by ~120 µatm and displayed high-amplitude variations of more than 50 µatm until 13.57 Ma. This transient rise in pCO_2 ended with a decrease to ~360 µatm and much reduced variability after 13.53 Ma

(Fig. 4E). Sea-surface pH values within the entire record range from 7.87 to 8.07± 0.05 (Figs. 4D and S1), while deep-sea

160 pH varies between 7.68 and 7.82 ± 0.07 over the same interval. Interestingly, the pH offset between the surface and deep ocean is nearly identical to the modern gradient and does not change substantially within our Miocene record (Fig. S1).

It is possible that the overall absolute pCO_2 values and the glacial rise after 13.82 Ma are overestimated by up to ~80 µatm and ~30 µatm, respectively, since pH might affect planktonic foraminiferal Mg/Ca and hence the sea-surface temperature estimations (Fig. S2) (Gray and Evans, 2019). Since differences in relative pCO_2 changes are not substantial and absolute

165 values are within uncertainties between both reconstructions, confirming the overall robustness of our pCO_2 record, we report the uncorrected data here.

The pCO_2 variations within the studied time interval show a remarkable agreement with variations in $\delta^{13}C$ that correspond to CM5b and CM6 (Fig. 5). Accordingly, the maxima at ~14.1 and 13.7 Ma as well as the minima at ~13.9 and 13.5 Ma indicate that atmospheric CO_2 levels were paced by the 400 k.y. eccentricity cycle, as also demonstrated by evolutive

170 harmonic and power spectral analyses (Fig. 6).

3.2 Sensitivity tests

Given that we propose an eccentricity-modulated change in TA input to the ocean, which might have affected our pCO_2 reconstruction, we carried out several sensitivity tests. The first tests demonstrate that either constant salinity, a ~1 unit change in salinity, or TA co-varying with salinity using a modern TA-S relationship, has no discernible effect on pCO_2

175 estimates (Fig. 7A). As ODP Site 1092 was apparently influenced by a northward migration of the Southern Ocean fronts, we tested the potential impact on calculated pCO_2 by varying TA with temperature. Even at an unrealistically high total change of 400 µmol/kg, calculated relative pCO_2 changes are very similar after the EAIS expansion at ~13.9 Ma (Fig. 7B). Given the modern sea-surface TA gradient across the polar frontal system of ~100 µmol/kg (higher in the south), we conclude that the increasing influence of southern-sourced surface waters on pCO_2 estimates at our study site is

180 comparatively small. When in our simulations TA was varied with pH or eccentricity (both on short and long periodicity) by ±100 µmol/kg, pCO_2 reconstructions are almost identical among each other (Figs. 7C-7H). On the other hand, at TA variations of ±400 µmol/kg, the pCO_2 estimates may differ substantially between the different scenarios, but the general shape of the record remains more or less the same. Given that total variations in TA of 800 µmol/kg are very unlikely, we suggest that periodic changes in monsoon-driven TA do not affect our pCO_2 estimates significantly.

185 ## 4. Discussion

4.1 Comparison with other pCO_2 records

Our pCO_2 data broadly agree with reconstructed long-term trends based on planktonic foraminiferal $\delta^{11}B$ (Foster et al., 2012) and paleosol $\delta^{13}C$ (Ji et al., 2018), despite a few differing values before CM5b and during CM6 (Fig. 3). The boron isotope

190 data from the Mediterranean Sea by Badger et al. (2013) also show decreasing pCO_2 values after 13.8 Ma, but no rebound after 13.75 Ma and no rise after 13.85 Ma, although these discrepancies may be due to the different sampling resolutions. In contrast, the pCO_2 reconstructions from high-resolution alkenone $\delta^{13}C$ data from Badger et al. (2013) are similar to the estimates of Super et al. (2018), which are considerably lower than the boron-based reconstructions and do not exhibit significant changes CM6. This might be related to the insensitivity of the alkenone proxy at low to moderate pCO_2 levels (Badger et al., 2019). It is worth noting that our pCO_2 record reveals a striking match with the box model output presented in

195 Ma et al. (2011), suggesting a linear response of weathering-controlled nutrient input to changes in orbital parameters with attendant variations in ocean carbon reservoir during the middle Miocene.

4.2 The role of eccentricity in the carbon cycle

The pCO_2 increase preceding and following the EAIS expansion closely tracks the global $\delta^{13}C$ history of CM5b and CM6 (Fig. 4), emphasizing a fundamental link between changes in the ocean carbon cycle and atmospheric carbon dioxide. The

200 CM peaks correspond to minima in the 400 k.y. eccentricity cycle, suggesting that $\delta^{13}C$ variations were related to changes in monsoon and weathering intensity (Holbourn et al., 2007; Ma et al., 2011). Monsoon intensity is paced by solar radiation variations caused by precessional cycles but their amplitude variations are modified by eccentricity. More precisely, higher eccentricity results in larger precession amplitudes and hence in larger wet/dry variations in the tropics (e.g., Wang, 2009), stronger physical and chemical weathering, and ultimately in an increased input of particulate organic material, dissolved

205 inorganic carbon, alkalinity and nutrients to the oceans (e.g., Clift and Plumb, 2008; Ma et al., 2011; Wan et al., 2009). The potential influence of alkalinity variations on our pCO_2 record is shown in Fig. 7 and evaluated in section 3.2.

The increased nutrient supply enhanced the primary production and organic carbon burial, which in turn lowered pCO_2. At the same time, the burial of shallow and total calcium carbonate ($CaCO_3$) increased, while $CaCO_3$ burial in the deep ocean decreased (Holbourn et al., 2007). However, as the net burial of $CaCO_3$ (enriched in ^{13}C) in relation to C_{org} (depleted in ^{13}C)

210 increased at high eccentricity, $\delta^{13}C_{DIC}$ values decreased, which is in line with the global isotope signature (Holbourn et al., 2007; Ma et al., 2011).

The increase in carbonate burial in shallow seas should have removed alkalinity from seawater, and thus lowered pH and released CO_2 to the atmosphere (e.g., Zeebe and Wolf-Gladrow, 2001) during 100 k.y. eccentricity maxima, but the resolution of our record is too low to detect this. On longer timescales (400 k.y. cycles), however, increased alkalinity input

215 from rivers, dissolution of deep-sea carbonates, and the enhanced burial of C_{org} in tropical regions during eccentricity maxima might have contributed to the long-term decrease in pCO_2. This agrees well with the box model output from Ma et al. (2011), suggesting that during the long-eccentricity maxima pCO_2 decreased when the monsoon was most intense and the organic carbon burial and river fluxes were high. Conversely, weathering and nutrient supply to the ocean in low latitudes decreased when eccentricity was low, resulting in a net decrease in the $CaCO_3$-to-C_{org} burial ratio and hence in CO_2 release

220 and higher $\delta^{13}C$.

Climate
of the Past
Discussions

4.3 Enhanced glacial deep-water ventilation

The MMCT bears similarities to the Eocene-Oligocene transition (EOT) ~34 Ma ago, when Antarctic ice-expansion was also accompanied by a large positive $\delta^{13}C$ excursion, in terms of both magnitude and duration (Coxall et al., 2005). The $\delta^{13}C$ excursion following Antarctic glaciation was accompanied by a transient pCO_2 rise of more than 300 µatm (Pearson et al.,

225   2009; Heureux and Rickaby, 2015), which bears similarity to the pCO_2 rise during the mid-Miocene EAIS expansion, although the amplitude was much larger. A modeling study suggested that a sea-level-fall-induced shelf-basin carbonate burial fractionation and a temporal enhancement of deep-water formation (by 150 %) in the Southern Ocean were sufficient to produce both the positive $\delta^{13}C$ excursion and a transient pCO_2 rise by ~80 µatm in the EOT (McKay et al., 2016). Similarly, ocean circulation may have intensified during the Miocene EAIS expansion, as the latitudinal temperature

230   gradient increased and atmospheric circulation strengthened. This is supported by benthic foraminifers, Mn/Ca and XRF data from Southeast Pacific sites, which indicate improved deep-water ventilation and carbonate preservation after 13.9 Ma, particularly during colder climate phases (Holbourn et al., 2013). Improved deep-water ventilation may also have led to enhanced advection of silica-rich waters toward low latitudes, culminating in an increased upwelling and diatom productivity between 14.04 and 13.96 Ma and between 13.84 and 13.76 Ma in the equatorial East Pacific, as indicated by massive opal

235   accumulation found at IODP Site U1338 (Holbourn et al., 2014). We speculate that increased upwelling may have resulted in CO_2 outgassing, if the supply exceeded consumption by primary productivity.

5. Conclusions

We conclude that pCO_2 variations across the MMCT were paced by 400 k.y. eccentricity cycles, where pCO_2 decreased at high eccentricity and rose when eccentricity was low (Fig. 4). At high eccentricity, the global monsoon and hence

240   weathering intensity increased (e.g., Wang, 2009), causing an increased input of dissolved inorganic carbon, alkalinity and nutrients to the oceans. The resulting increase in the $CaCO_3$-to-C_{org} burial ratio lowered pCO_2 and decreased $\delta^{13}C_{DIC}$. The pCO_2 decrease between 14.08 and 13.87 Ma might have facilitated the initiation of EAIS expansion starting at ~13.9 Ma. Conversely, the CO_2 rise after the onset of EAIS expansion, possibly caused by decreased weathering fluxes at low eccentricity and hence net decrease in the $CaCO_3$-to-C_{org} burial ratio, could have acted as a negative feedback on the

245   progressing Antarctic glaciation. In this way, the radiative forcing due to the temporary pCO_2 rise may have helped to stabilize the climate system on its way to the late Cenozoic "icehouse" world. Our results also highlight the need for more high-resolution pCO_2 records across the middle Miocene climate transition.

Data availability

The boron isotope data collected for this study are available from Table S1, the tie points used for the revised age model are

250   listed in Table S2, and the modified R code of 'MgCaRB' (Gray and Evans, 2019) is available from S1 in the supplement.

Author contribution

MR and JB conceived the study (conceptualization). MR carried out measurements, analyzed the data, and performed data statistics (data curation, formal analysis, investigation). JB provided access to analytical instruments at AWI (resources). MR raised funding for the project (funding acquisition). MR produced the figures for the manuscript (visualization), and wrote
255   the first draft of the mansucript (writing – original draft). All authors interpreted, edited, and reviewed the manuscript (writing – review & editing).

Competing interests

The authors declare that they have no conflict of interest.

Acknowledgement

References

265   Abels, H. A., Hilgen, F. J., Krijgsman, W., Kruk, R. W., Raffi, I., Turco, E. and Zachariasse, W. J.: Long-period orbital control on middle Miocene global cooling: Integrated stratigraphy and astronomical tuning of the Blue Clay Formation on Malta, Paleoceanography, 20, PA4012, doi:10.1029/2004PA001129, 2005.

Badger, M. P. S., Lear, C. H., Pancost, R. D., Foster, G. L., Bailey, T. R., Leng, M. J. and Abels, H. A.: CO_2 drawdown following the middle Miocene expansion of the Antarctic Ice Sheet, Paleoceanography, 28(1), 42–53,
270   doi:10.1002/palo.20015, 2013.

Badger, M. P. S., Chalk, T. B., Foster, G. L., Bown, P. R., Gibbs, S. J., Sexton, P. F., Schmidt, D. N., Pälike, H., Mackensen, A. and Pancost, R. D.: Insensitivity of alkenone carbon isotopes to atmospheric CO_2 at low to moderate CO_2 levels, Clim. Past, 15(2), 539–554, doi:https://doi.org/10.5194/cp-15-539-2019, 2019.

Barker, S., Greaves, M. and Elderfield, H.: A study of cleaning procedures used for foraminiferal Mg/Ca paleothermometry,
275   Geochem. Geophys. Geosyst., 4(9), 8407, doi:10.1029/2003GC000559, 2003.

Caves, J. K., Jost, A. B., Lau, K. V. and Maher, K.: Cenozoic carbon cycle imbalances and a variable weathering feedback, Earth Planet. Sci. Lett., 450, 152–163, doi:10.1016/j.epsl.2016.06.035, 2016.

Censarek, B. and Gersonde, R.: Miocene diatom biostratigraphy at ODP Sites 689, 690, 1088, 1092 (Atlantic sector of the Southern Ocean), Mar. Micropaleontol., 45(3–4), 309–356, doi:10.1016/S0377-8398(02)00034-8, 2002.
280   Clift, P. D. and Plumb, R. A.: The Asian Monsoon: Causes, History and Effects, Cambridge University Press., 2008.

Coxall, H. K., Wilson, P. A., Palike, H., Lear, C. H. and Backman, J.: Rapid stepwise onset of Antarctic glaciation and deeper calcite compensation in the Pacific Ocean, Nature, 433(7021), 53–57, doi:10.1038/nature03135, 2005.

Evans, D. and Müller, W.: Deep time foraminifera Mg/Ca paleothermometry: Nonlinear correction for secular change in seawater Mg/Ca, Paleoceanography, 27(4), doi:10.1029/2012PA002315, 2012.

285 Flower, B. P. and Kennett, J. P.: Middle Miocene ocean-climate transition: High-resolution oxygen and carbon isotopic records from Deep Sea Drilling Project Site 588A, southwest Pacific, Paleoceanography, 8(6), 811–843, doi:10.1029/93PA02196, 1993.

Flower, B. P. and Kennett, J. P.: The middle Miocene climatic transition: East Antarctic ice sheet development, deep ocean circulation and global carbon cycling, Paleogeogr. Paleoclimatol. Paleoecol., 108, 537–555, 290 doi:https://doi.org/10.1016/0031-0182(94)90251-8, 1994.

Foster, G. L., Lear, C. H. and Rae, J. W. B.: The evolution of pCO$_2$, ice volume and climate during the middle Miocene, Earth Planet. Sci. Lett., 341–344, 243–254, doi:10.1016/j.epsl.2012.06.007, 2012.

Goyet, C., Healy, R., Ryan, J. and Kozyr, A.: Global Distribution of Total Inorganic Carbon and Total Alkalinity below the Deepest Winter Mixed Layer Depths, ORNL/CDIAC-127, NDP-076. Carbon Dioxide Information Analysis Center, Oak 295 Ridge National Laboratory, U.S. Department of Energy, Oak Ridge, Tennessee. [online] Available from: https://digital.library.unt.edu/ark:/67531/metadc724552/m1/7/ (Accessed 18 May 2017), 2000.

Gray, W. R. and Evans, D.: Nonthermal Influences on Mg/Ca in Planktonic Foraminifera: A Review of Culture Studies and Application to the Last Glacial Maximum, Paleocean. Paleoclimat., 34(3), 306–315, doi:10.1029/2018PA003517, 2019.

Greenop, R., Foster, G. L., Wilson, P. A. and Lear, C. H.: Middle Miocene climate instability associated with high-amplitude 300 CO$_2$ variability, Paleoceanography, 29(9), 2014PA002653, doi:10.1002/2014PA002653, 2014.

Greenop, R., Hain, M. P., Sosdian, S. M., Oliver, K. I. C., Goodwin, P., Chalk, T. B., Lear, C. H., Wilson, P. A. and Foster, G. L.: A record of Neogene seawater δ^{11}B reconstructed from paired δ^{11}B analyses on benthic and planktic foraminifera, Clim. Past, 13(2), 149–170, doi:10.5194/cp-13-149-2017, 2017.

Heureux, A. M. C. and Rickaby, R. E. M.: Refining our estimate of atmospheric CO$_2$ across the Eocene–Oligocene climatic 305 transition, Earth Planet. Sci. Lett., 409, 329–338, doi:10.1016/j.epsl.2014.10.036, 2015.

Holbourn, A., Kuhnt, W., Simo, J. A. (Toni) and Li, Q.: Middle Miocene isotope stratigraphy and paleoceanographic evolution of the northwest and southwest Australian margins (Wombat Plateau and Great Australian Bight), Paleogeogr. Paleoclimatol. Paleoecol., 208(1), 1–22, doi:10.1016/j.palaeo.2004.02.003, 2004.

Holbourn, A., Kuhnt, W., Schulz, M. and Erlenkeuser, H.: Impacts of orbital forcing and atmospheric carbon dioxide on 310 Miocene ice-sheet expansion, Nature, 438, 483–487, doi:https://doi.org/10.1038/nature04123, 2005.

Holbourn, A., Kuhnt, W., Schulz, M., Flores, J.-A. and Andersen, N.: Orbitally-paced climate evolution during the middle Miocene "Monterey" carbon-isotope excursion, Earth Planet. Sci. Lett., 261, 534–550, doi:https://doi.org/10.1016/j.epsl.2007.07.026, 2007.

Holbourn, A., Kuhnt, W., Frank, M. and Haley, B. A.: Changes in Pacific Ocean circulation following the Miocene onset of 315 permanent Antarctic ice cover, Earth and Planetary Science Letters, 365, 38–50, doi:10.1016/j.epsl.2013.01.020, 2013.

Holbourn, A., Kuhnt, W., Lyle, M., Schneider, L., Romero, O. and Andersen, N.: Middle Miocene climate cooling linked to intensification of eastern equatorial Pacific upwelling, Geology, 42(1), 19–22, doi:10.1130/G34890.1, 2014.

Horita, J., Zimmermann, H. and Holland, H. D.: Chemical evolution of seawater during the Phanerozoic: Implications from the record of marine evaporites, Geochim. Cosmochim. Acta, 66(21), 3733–3756, doi:10.1016/S0016-7037(01)00884-5, 320 2002.

Ji, S., Nie, J., Lechler, A., Huntington, K. W., Heitmann, E. O. and Breecker, D. O.: A symmetrical CO_2 peak and asymmetrical climate change during the middle Miocene, Earth Planet. Sci. Lett., 499, 134–144, doi:10.1016/j.epsl.2018.07.011, 2018.

Jonkers, L. and Kučera, M.: Global analysis of seasonality in the shell flux of extant planktonic Foraminifera, 325 Biogeosciences, 12(7), 2207–2226, doi:10.5194/bg-12-2207-2015, 2015.

Kuhnert, H., Bickert, T. and Paulsen, H.: Southern Ocean frontal system changes precede Antarctic ice sheet growth during the middle Miocene, Earth Planet. Sci. Lett., 284(3–4), 630–638, doi:10.1016/j.epsl.2009.05.030, 2009.

Kürschner, W. M., Kvaček, Z. and Dilcher, D. L.: The impact of Miocene atmospheric carbon dioxide fluctuations on climate and the evolution of terrestrial ecosystems, PNAS, 105(2), 449–453, doi:https://doi.org/10.1073/pnas.0708588105, 330 2008.

Laskar, J., Robutel, P., Joutel, F., Gastineau, M., Correia, A. C. M. and Levrard, B.: A long-term numerical solution for the insolation quantities of the Earth, Astron. Astrophys., 428(1), 25, doi:10.1051/0004-6361:20041335, 2004.

Lavigne, H., Epitalon, J.-M. and Gattuso, J.-P.: seacarb: seawater carbonate chemistry with R. [online] Available from: http://CRAN.R-project.org/package=seacarb, 2011.

335 Lemarchand, D., Gaillardet, J., Lewin, É. and Allègre, C. J.: The influence of rivers on marine boron isotopes and implications for reconstructing past ocean pH, Nature, 408, 951–954, doi:10.1038/35050058, 2000.

Lear, C. H., Rosenthal, Y., Coxall, H. K. and Wilson, P. A.: Late Eocene to early Miocene ice sheet dynamics and the global carbon cycle, Paleoceanography, 19, PA4015, doi:10.1029/2004PA001039, 2004.

Ma, W., Tian, J., Li, Q. and Wang, P.: Simulation of long eccentricity (400-kyr) cycle in ocean carbon reservoir during 340 Miocene Climate Optimum: Weathering and nutrient response to orbital change, Geophys. Res. Lett., 38(10), doi:10.1029/2011GL047680, 2011.

Ma, X., Tian, J., Ma, W., Li, K. and Yu, J.: Changes of deep Pacific overturning circulation and carbonate chemistry during middle Miocene East Antarctic ice sheet expansion, Earth Planet. Sci. Lett., 484, 253–263, doi:10.1016/j.epsl.2017.12.002, 2018.

345 Mashiotta, T. A., Lea, D. W. and Spero, H. J.: Glacial-interglacial changes in Subantarctic sea surface temperature and $\delta^{18}O$-water using foraminiferal Mg, Earth Planet. Sci Lett., 170, 417–432, doi:10.1016/S0012-821X(99)00116-8, 1999.

McKay, D. I. A., Tyrrell, T. and Wilson, P. A.: Global carbon cycle perturbation across the Eocene-Oligocene climate transition, Paleoceanography, 31(2), 311–329, doi:10.1002/2015PA002818, 2016.

Misra, S., Owen, R., Kerr, J., Greaves, M. and Elderfield, H.: Determination of $\delta^{11}B$ by HR-ICP-MS from mass limited 350 samples: Application to natural carbonates and water samples, Geochim. Cosmochim. Acta, 140, 531–552, doi:10.1016/j.gca.2014.05.047, 2014.

Mortyn, P. G. and Charles, C. D.: Planktonic foraminiferal depth habitat and $\delta^{18}O$ calibrations: Plankton tow results from the Atlantic sector of the Southern Ocean, Paleoceanography, 18(2), 1037, doi:10.1029/2001PA000637, 2003.

355 Myers, S. R.: Astrochron: An R Package for Astrochronology. [online] Available from: https://cran.r-project.org/package=astrochron, 2014.

Pagani, M., Freeman, K. H. and Arthur, M. A.: Late Miocene Atmospheric CO_2 Concentrations and the Expansion of C4 Grasses, Science, 285, 876–879, doi:10.1126/science.285.5429.876, 1999.

Pearson, P. N. and Palmer, M. R.: Atmospheric carbon dioxide concentrations over the past 60 million years, Nature, 406, 695–699, doi:10.1038/35021000, 2000.

360 Pearson, P. N., Foster, G. L. and Wade, B. S.: Atmospheric carbon dioxide through the Eocene–Oligocene climate transition, Nature, 461(7267), 1110–1113, doi:10.1038/nature08447, 2009.

Rae, J. W. B., Foster, G. L., Schmidt, D. N. and Elliott, T.: Boron isotopes and B/Ca in benthic foraminifera: Proxies for the deep ocean carbonate system, Earth Planet. Sci. Lett., 302(3–4), 403–413, doi:10.1016/j.epsl.2010.12.034, 2011.

Raitzsch, M. and Hönisch, B.: Cenozoic boron isotope variations in benthic foraminifers, Geology, 41(5), 591–594,
365 doi:https://doi.org/10.1130/G34031.1, 2013.

Raitzsch, M., Kuhnert, H., Groeneveld, J. and Bickert, T.: Benthic foraminifer Mg/Ca anomalies in South Atlantic core top sediments and their implications for paleothermometry, Geochem. Geophys. Geosyst., 9(5), Q05010, doi:https://doi.org/10.1029/2007GC001788, 2008.

Raitzsch, M., Bijma, J., Benthien, A., Richter, K.-U., Steinhoefel, G. and Kučera, M.: Boron isotope-based seasonal paleo-
370 pH reconstruction for the Southeast Atlantic – A multispecies approach using habitat preference of planktonic foraminifera, Earth Planet. Sci. Lett., 487, 138–150, doi:https://doi.org/10.1016/j.epsl.2018.02.002, 2018.

Ridgwell, A.: A Mid Mesozoic Revolution in the regulation of ocean chemistry, Mar. Geol., 217(3–4), 339–357, doi:16/j.margeo.2004.10.036, 2005.

Shackleton, N. J.: Attainment of isotopic equilibrium between ocean water and the benthonic foraminifera genus *Uvigerina*:
375 isotopic changes in the ocean during the last glacial, Cent. Nat. Rech. Sci. Colloq. Int., 219, 203–209, 1974.

Shevenell, A. E. and Kennett, J. P.: Paleoceanographic Change During the Middle Miocene Climate Revolution: An Antarctic Stable Isotope Perspective, in The Cenozoic Southern Ocean: Tectonics, Sedimentation, and Climate Change Between Australia and Antarctica, pp. 235–251, American Geophysical Union (AGU)., 2004.

Shevenell, A. E., Kennett, J. P. and Lea, D. W.: Middle Miocene Southern Ocean Cooling and Antarctic Cryosphere
380 Expansion, Science, 305, 1766–1770, doi:10.1126/science.1100061, 2004.

Shevenell, A. E., Kennett, J. P. and Lea, D. W.: Middle Miocene ice sheet dynamics, deep-sea temperatures, and carbon cycling: A Southern Ocean perspective, Geochem. Geophys. Geosyst., 9(2), Q02006, doi:10.1029/2007GC001736, 2008.

Sosdian, S. M., Greenop, R., Hain, M. P., Foster, G. L., Pearson, P. N. and Lear, C. H.: Constraining the evolution of Neogene ocean carbonate chemistry using the boron isotope pH proxy, Earth Planet. Sci. Lett., 498, 362–376,
385 doi:10.1016/j.epsl.2018.06.017, 2018.

Spratt, R. M. and Lisiecki, L. E.: A Late Pleistocene sea level stack, Clim. Past, 12(4), 1079–1092, doi:https://doi.org/10.5194/cp-12-1079-2016, 2016.

Stanley, S. M. and Hardie, L. A.: Hypercalcification: Paleontology links plate tectonics and geochemistry to sedimentology, GSA Today, 9, 2–7, 1999.

Climate
of the Past
Discussions

Open Access

EGU

390 Super, J. R., Thomas, E., Pagani, M., Huber, M., O'Brien, C. and Hull, P. M.: North Atlantic temperature and pCO$_2$ coupling in the early-middle Miocene, Geology, 46(6), 519–522, doi:10.1130/G40228.1, 2018.

Takahashi, T., Olafsson, J., Goddard, J. G., Chipman, D. W. and Sutherland, S. C.: Seasonal variation of CO$_2$ and nutrients in the high-latitude surface oceans: A comparative study, Glob. Biogeochem. Cyc., 7(4), 843–878, doi:10.1029/93GB02263, 1993.

395 Takahashi, T., Sutherland, S. C., Wanninkhof, R., Sweeney, C., Feely, R. A., Chipman, D. W., Hales, B., Friederich, G., Chavez, F., Sabine, C., Watson, A., Bakker, D. C. E., Schuster, U., Metzl, N., Yoshikawa-Inoue, H., Ishii, M., Midorikawa, T., Nojiri, Y., Körtzinger, A., Steinhoff, T., Hoppema, M., Olafsson, J., Arnarson, T. S., Tilbrook, B., Johannessen, T., Olsen, A., Bellerby, R., Wong, C. S., Delille, B., Bates, N. R. and de Baar, H. J. W.: Climatological mean and decadal change in surface ocean pCO$_2$, and net sea–air CO$_2$ flux over the global oceans, Deep-Sea Res. II, 56(8–10), 554–577,
400 doi:10.1016/j.dsr2.2008.12.009, 2009.

Tyrrell, T. and Zeebe, R. E.: History of carbonate ion concentration over the last 100 million years, Geochim. Cosmochim. Acta, 68(17), 3521–3530, doi:10.1016/j.gca.2004.02.018, 2004.

Vincent, E. and Berger, W. H.: Carbon dioxide and polar cooling in the Miocene: the Monterey hypothesis, in The Carbon Cycle and Atmospheric CO$_2$: Natural Variations Archean to Present, pp. 455–468, American Geophysical Union,
405 Washington, DC. [online] Available from: https://doi.org/10.1029/GM032p0455, 1985.

Wan, S., Kürschner, W. M., Clift, P. D., Li, A. and Li, T.: Extreme weathering/erosion during the Miocene Climatic Optimum: Evidence from sediment record in the South China Sea, Geophys. Res. Lett., 36(19), doi:10.1029/2009GL040279, 2009.

Wang, B.-S., You, C.-F., Huang, K.-F., Wu, S.-F., Aggarwal, S. K., Chung, C.-H. and Lin, P.-Y.: Direct separation of boron
410 from Na- and Ca-rich matrices by sublimation for stable isotope measurement by MC-ICP-MS, Talanta, 82(4), 1378–1384, doi:10.1016/j.talanta.2010.07.010, 2010.

Wang, P.: Global monsoon in a geological perspective, Chin. Sci. Bull., 54(7), 1113–1136, doi:10.1007/s11434-009-0169-4, 2009.

Wright, J. D., Miller, K. G. and Fairbanks, R. G.: Early and Middle Miocene stable isotopes: Implications for Deepwater
415 circulation and climate, Paleoceanography, 7(3), 357–389, doi:10.1029/92PA00760, 1992.

Woodruff, F. and Savin, S.: Mid-Miocene isotope stratigraphy in the deep sea: high resolution correlations, paleoclimatic cycles, and sediment preservation, Paleoceanography, 6, 755–806, doi:https://doi.org/10.1029/91PA02561, 1991.

Zeebe, R. E. and Tyrrell, T.: History of carbonate ion concentration over the last 100 million years II: Revised calculations and new data, Geochim. Cosmochim. Acta, 257, 373–392, doi:10.1016/j.gca.2019.02.041, 2019.

420 Zeebe, R. E. and Wolf-Gladrow, D. A.: CO$_2$ in Seawater: Equilibrium, Kinetics, Isotopes, Elsevier Oceanography Series, Amsterdam., 2001.
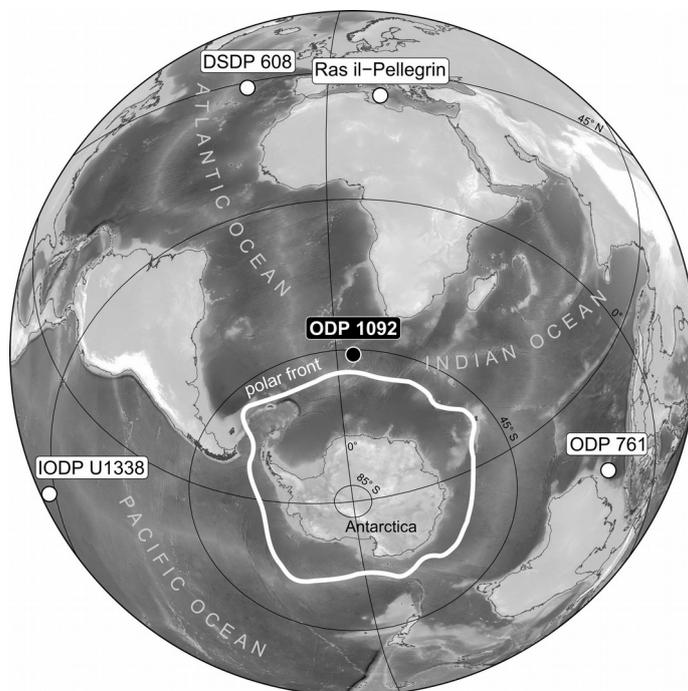
Figure 1: Azimuthal view of the location of ODP Site 1092 (water depth 1973 m) on the Meteor Rise in the South Atlantic Ocean, north of the modern polar front. Also shown are locations of DSDP Site 608, ODP Site 761, IODP Site U1338 and Ras-il-Pellegrin on Malta, for which pCO$_2$ records are displayed in Fig. 5.

425
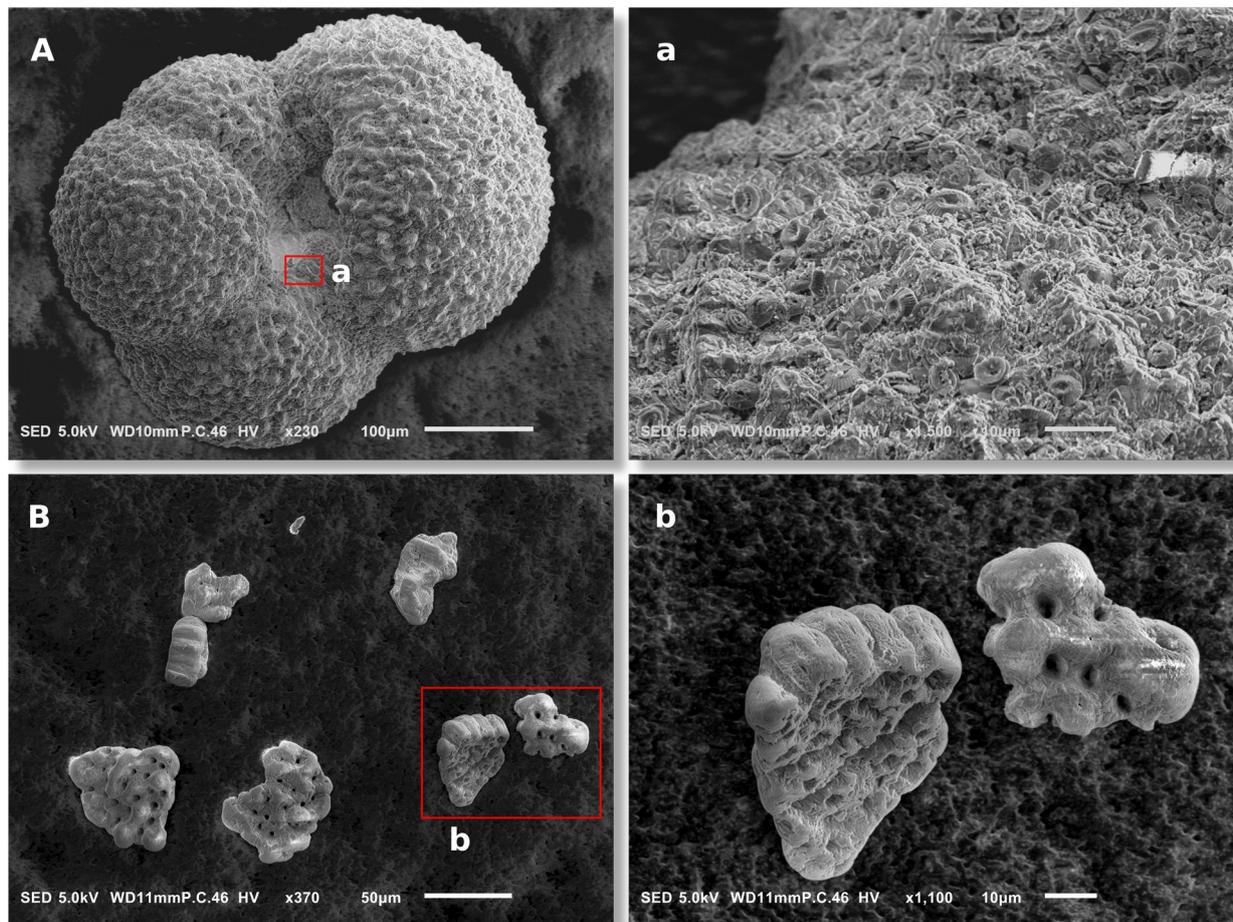
Figure 2. SEM images of collected *G. bulloides* for δ¹¹B analysis (representative example from 177-1092B-18-4, 69-71 cm). (A) Whole shell; (a) close-up image reveal intact coccoliths covering the shell surface indicating lack of post-depositional dissolution. (B) Shell fragments after chemical cleaning; (b) close-up image shows absence of non-shell material.
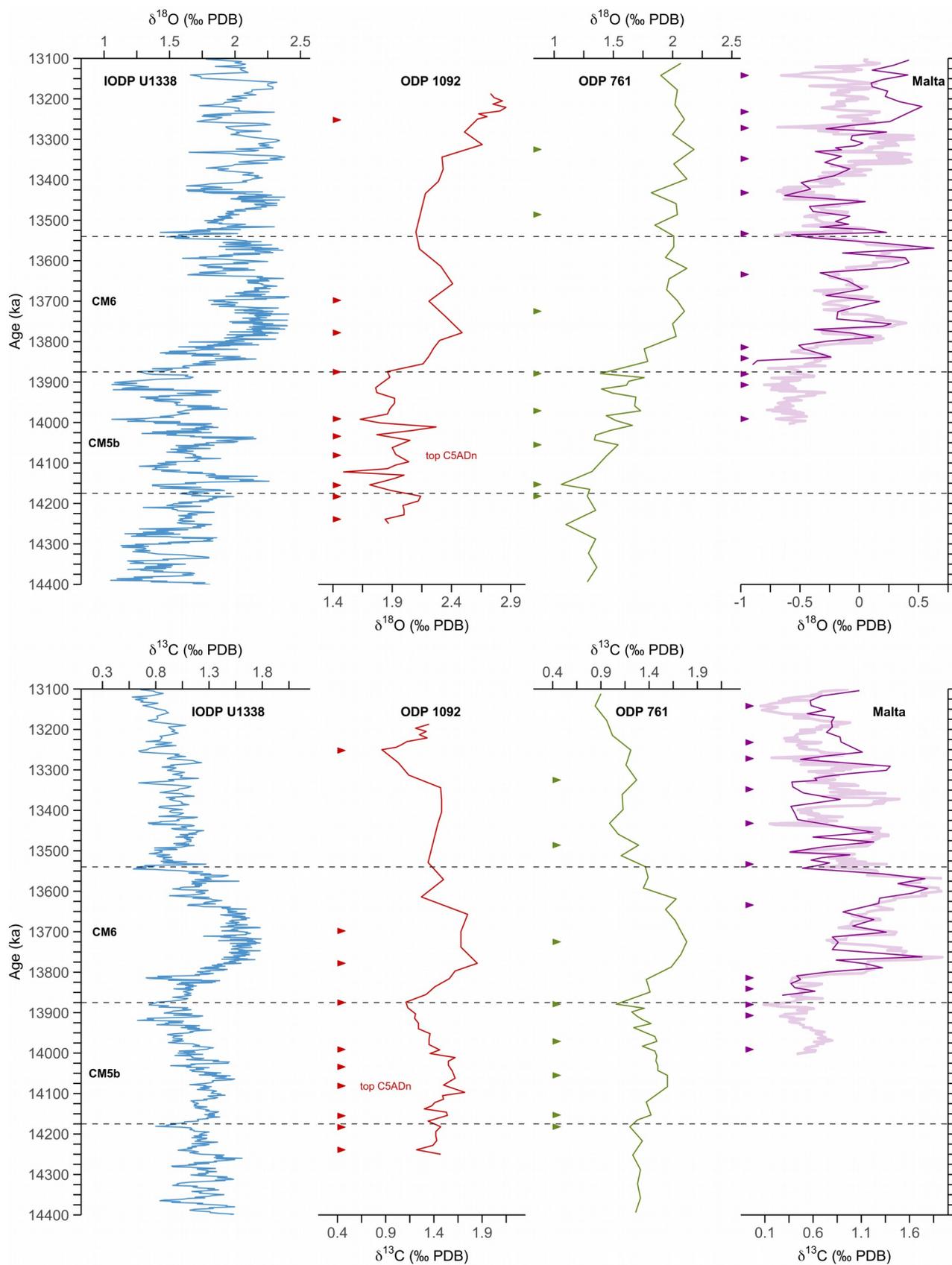
430 **Figure 3. Age models of ODP Site 1092, ODP Site 761 and Blue Clay Formation (Ras-il-Pellegrin, Malta), which were re-tuned with respect to the reference curve of IODP Site U1338 (Holbourn et al., 2014), based on their δ^{18}O (upper panel) and δ^{13}C (lower panel) records. Thick line of the Ras-il-Pellegrin record is from Abels et al. (2005), and thin line from Badger et al. (2015). Arrows mark tie points from this study, which are listed in Table S2. Dashed lines delimit CM events 5b and 6.**
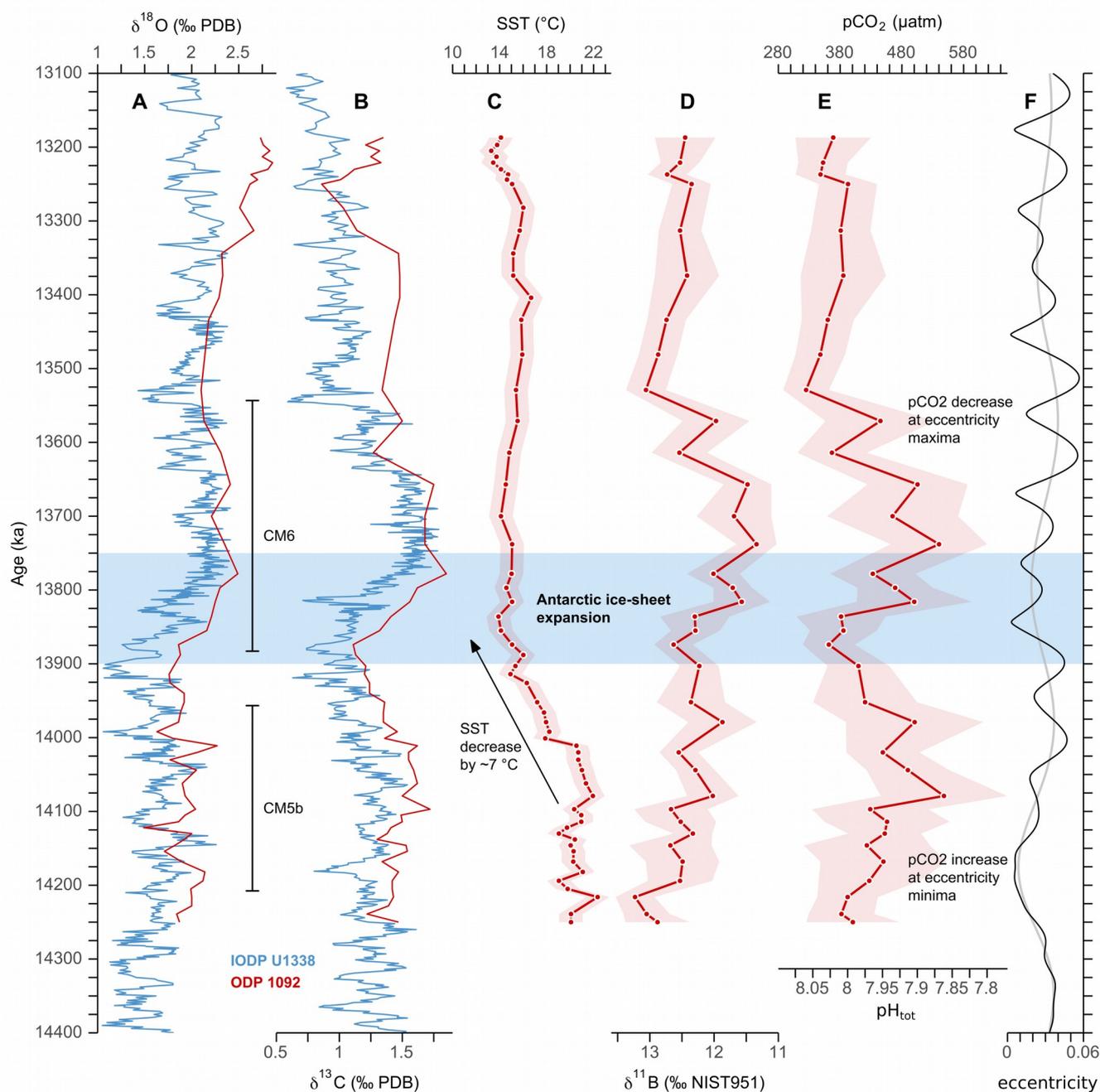
Figure 4. Proxy records of the middle Miocene climate transition. (A) Benthic oxygen isotope curve from ODP Site 1092 (in red) used in this study and from eastern Pacific IODP Site U1338 (in blue) used as a reference (Holbourn et al., 2014). (B) The same as in A) but for carbon isotopes. The carbon maximum events CM5b and CM6 are indicated. (C) Site 1092 sea-surface temperatures reconstructed from *G. bulloides* Mg/Ca ratios (Kuhnert et al., 2009), with ±1 °C uncertainty band. (D) Raw boron isotope data of *G. bulloides*. Shaded area indicates 2σ uncertainties of measurement. (E) Estimated *p*CO₂ of surface waters (derived from) using pH derived from (D), a total alkalinity (TA) of 2000 ± 100 µmol/kg, and a δ¹¹Bₛw value of 37.80 ‰. Secondary axis represents pH,

and shaded area delimits fully propagated pCO$_2$ uncertainties (). (F) Eccentricity of the Earth's orbit from Laskar et al. (2004) and lowpass-filtered 400 k.y. signal (grey line).
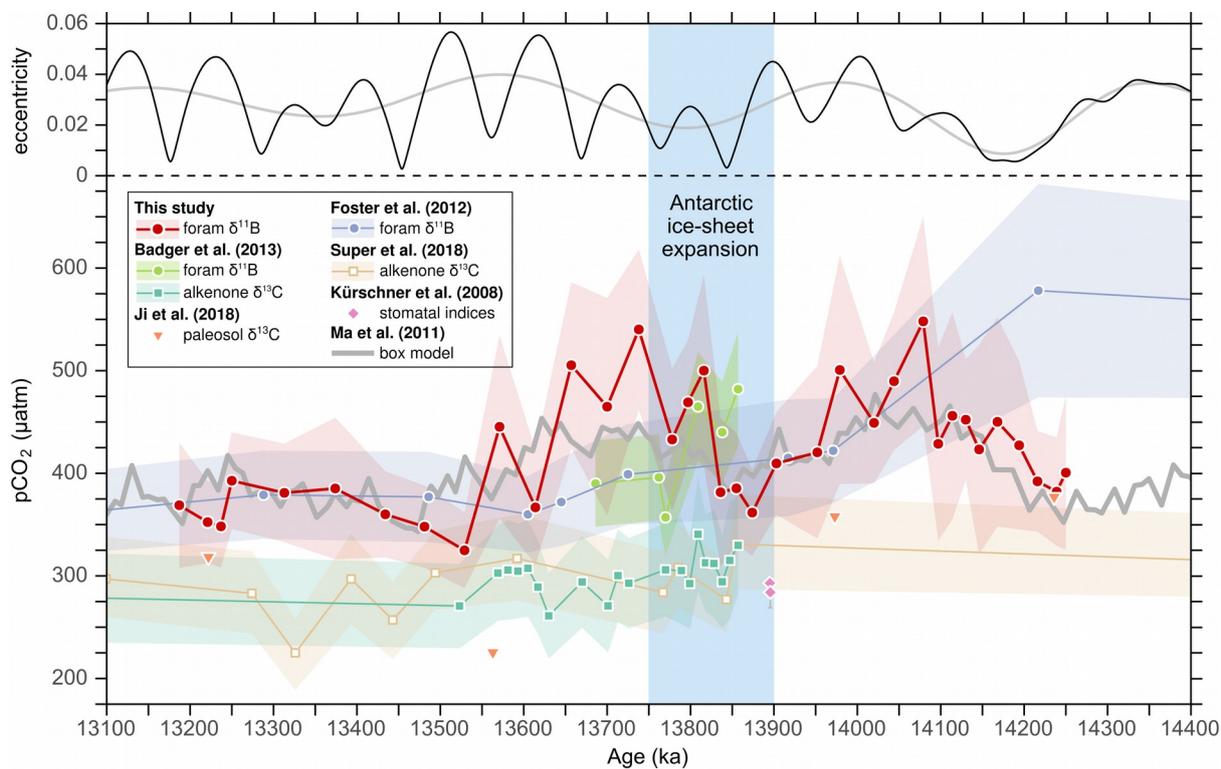
Figure 5. Eccentricity of the Earth's orbit from Laskar et al. (2004) (upper panel) and comparison of pCO$_2$ estimates from this study with literature data (lower panel). Note that the boron-based pCO$_2$ data from Foster et al. (2012) and Badger et al. (2013) were re-calculated using a TA of 2000 µmol/kg and a δ^{11}B$_{sw}$ value of 37.80 ‰ for consistency with our data. In addition, the age models from these studies were also revised for direct comparison with our record (Fig. 3). All other records are based on their original data and age models.
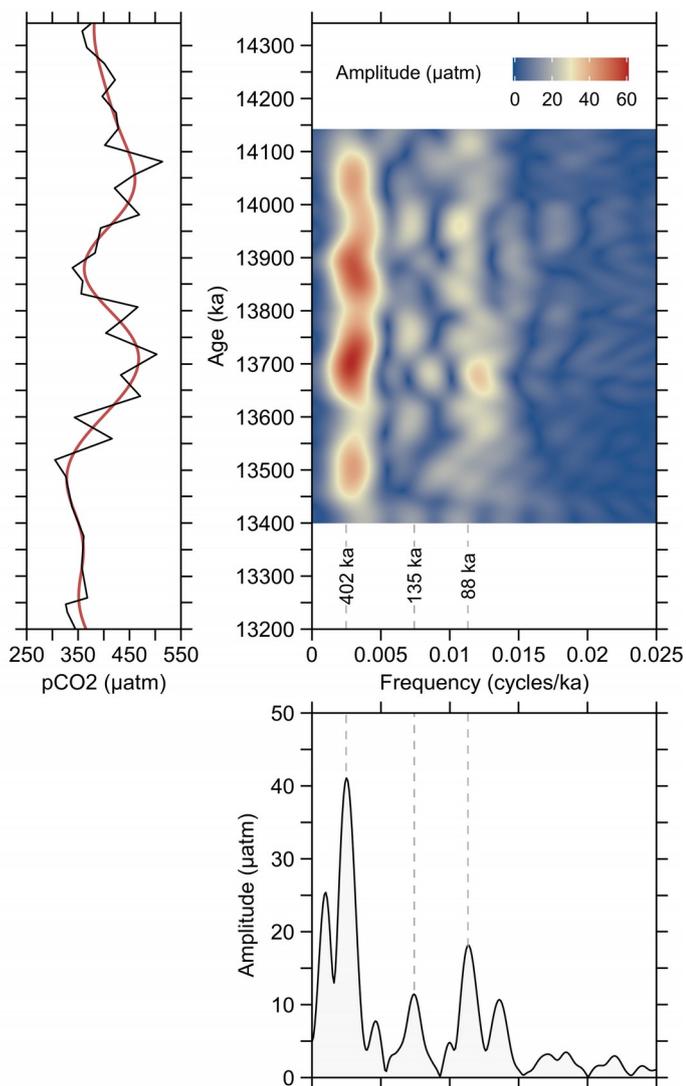
Figure 6. Evolutive harmonic analysis (EHA) and power spectral analysis of pCO_2 record from ODP Site 1092, using the Thomson multitaper method (MTM). The red line in the left panel is the lowpass-filtered 400 k.y. signal using cosine-tapered window. Analyses were performed using the R package 'Astrochron' (Myers, 2014).
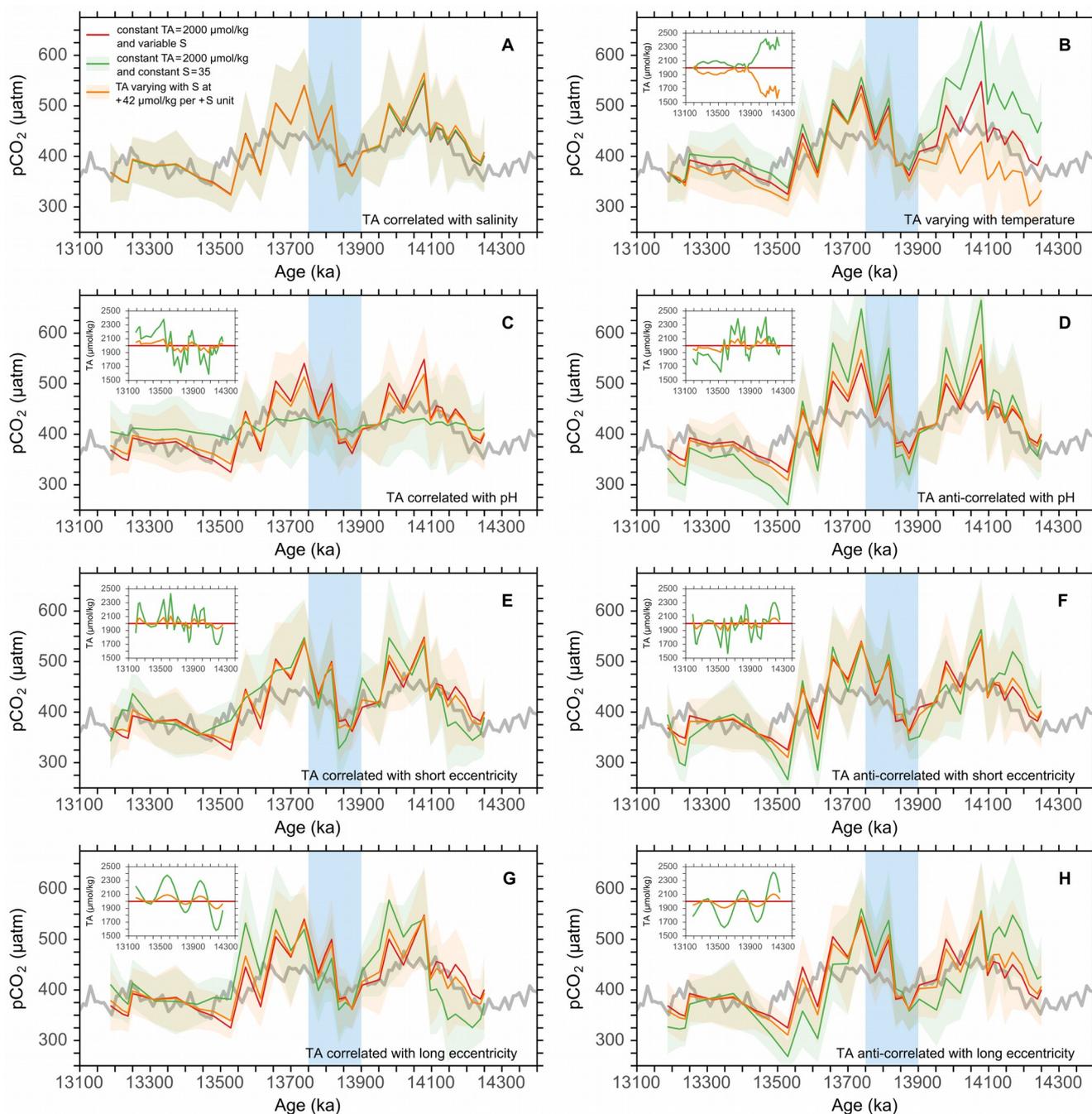
Figure 7. Sensitivity tests of pH-derived pCO₂ estimations. (A) Effect of varying salinity (derived from δ¹⁸O changes) and TA (at modern correlation with S) on estimated pCO₂. (B) Effect of TA on pCO₂ estimates, when TA is correlated (green) or anti-correlated (orange) with sea-surface temperature at a total range of 400 µmol/kg. (C-H) Effect of TA on pCO₂ estimates, when TA is (anti-)correlated with pH or eccentricity at maximum ranges of ±100 (orange) and ±400 µmol/kg (green). The grey line in all panels represents the box model output from Ma et al. (2011). Shaded areas represent propagated 2σ uncertainties. Note that the red line is the record shown in Figs. 4E and 5.

455